ACS APPLIED MATERIALS & INTERFACES

Research Article

Cite This: ACS Appl. Mater. Interfaces 2018, 10, 1646−1653

www.acsami.org

Polymer-Templated $LiFePO_4$/C Nanonetworks as High-Performance Cathode Materials for Lithium-Ion Batteries

Michael G. Fischer,[†] Xiao Hua,*[,†] Bodo D. Wilts,[†] Elizabeth Castillo-Martínez,[‡] and Ullrich Steiner*[,†]

[†]Adolphe Merkle Institute, Université de Fribourg, Chemin des Verdiers 4, 1700 Fribourg, Switzerland

[‡]Department of Chemistry, University of Cambridge, Lensfield Road, Cambridge CB2 1EW, U.K.

Supporting Information

ABSTRACT: Lithium iron phosphate (LFP) is currently one of the main cathode materials used in lithium-ion batteries due to its safety, relatively low cost, and exceptional cycle life. To overcome its poor ionic and electrical conductivities, LFP is often nanostructured, and its surface is coated with conductive carbon (LFP/C). Here, we demonstrate a sol−gel based synthesis procedure that utilizes a block copolymer (BCP) as a templating agent and a homopolymer as an additional carbon source. The high-molecular-weight BCP produces self-assembled aggregates with the precursor-sol on the 10 nm scale, stabilizing the LFP structure during crystallization at high temperatures. This results in a LFP nanonetwork consisting of interconnected ∼10 nm-sized particles covered by a uniform carbon coating that displays a high rate performance and an excellent cycle life. Our "one-pot" method is facile and scalable for use in established battery production methodologies.

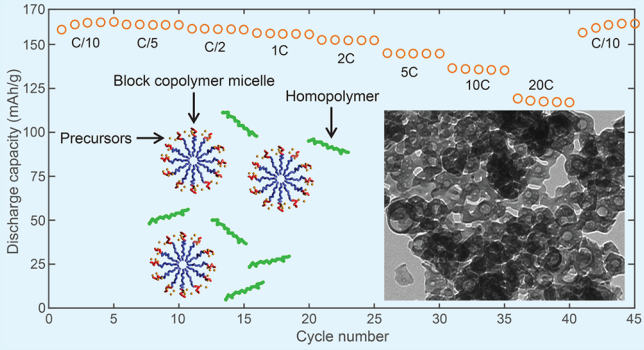

KEYWORDS: *self-assembly, battery, sol−gel, block copolymer, lithium iron phosphate, nanostructures*

1. INTRODUCTION

Lithium-ion batteries (LIBs) have attracted much interest over the past decades due to their pivotal role in consumer electronics. The increasing demand for grid storage driven by the development of renewable energies and the market growth for (hybrid) electric vehicles indicate that LIBs will be of even greater importance in the future. In contrast to their application in portable devices, batteries for these emerging technologies require not only high energy and power densities but also long cycle lives and high safety standards.[1−5]

Despite its somewhat lower energy density compared to other commercialized cathode materials (e.g., $LiNi_{1/3}Mn_{1/3}Co_{1/3}O_2$),[4] $LiFePO_4$ (LFP) represents one of the most promising cathode materials due to its superior cyclability and inherent safety.[5] It is noteworthy that the material was originally envisioned only for low-power applications[6] due to its low ionic diffusivity and poor electrical conductivity.[7,8] While there has been some success in increasing these properties via controlled off-stoichiometry[9] and doping,[7] most research focuses on structural designs that provide efficient pathways for electronic and ionic transport.

Coating LFP particles with conductive carbon (termed LFP/C) is the predominant way to enhance electrical conduction within an insulating LFP cathode.[10,11] Other approaches combined LFP with additional carbon materials, e.g., tailored carbon structures,[12−15] carbon nanotubes,[16,17] and graphene.[18] Nevertheless, most LFP materials still rely on thin, uniform carbon coatings[5] with a high degree of graphitization to increase the electrical conductivity of the carbon layer.[19]

Addressing the low ionic conductivity of LFP requires reducing diffusion distances within the active material. Nanostructured LFP electrodes are therefore widely employed.[3,5] Their large surface area further facilitates fast charge transfer across the electrode/electrolyte interface.[1,5,20] Early work utilized simple sol−gel processes that formed (irregularly shaped) nanosized[21] and meso/macroporous materials.[22] Significant improvements in rate performance were achieved for LFP nanoparticles,[23−25] but electrodes made of nanoparticles suffer from low volumetric energy densities.[1,5] Hydro and solvothermal synthesis methods present an alternative approach that affords morphological control,[4,5] as demonstrated by the fabrication of diverse morphologies with short diffusion distances, such as nanoplates and nanoparticles,[26−29] porous microspheres,[30,31] submicrometer-sized hollow particles,[32−35] and nanowires.[36] A limitation of using low-temperature hydrothermal methods alone is their tendency to form defects in the crystal structure, which hinders Li^+ transport and adversely affects the electrochemical perform-

Received: August 18, 2017
Accepted: December 21, 2017
Published: December 21, 2017

DOI: 10.1021/acsami.7b12376
ACS Appl. Mater. Interfaces 2018, 10, 1646−1653

ance.[37] LFP/C composites created by the infiltration of precursor solutions into meso/macroporous templates[38−40] and by the replication of hard templates[41−43] demonstrated various well-defined morphologies. While some of these nanostructures resulted in excellent rate capabilities, their fabrication usually requires multiple complicated processing steps, impeding scalability on an industrial scale.

In this article, we demonstrate a novel concept for the facile and scalable fabrication of a high-performance nanostructured LFP/C cathode material.

2. RESULTS AND DISCUSSION

2.1. Structure Formation. The employed process is outlined in Figure 1 (see Experimental Section for details).

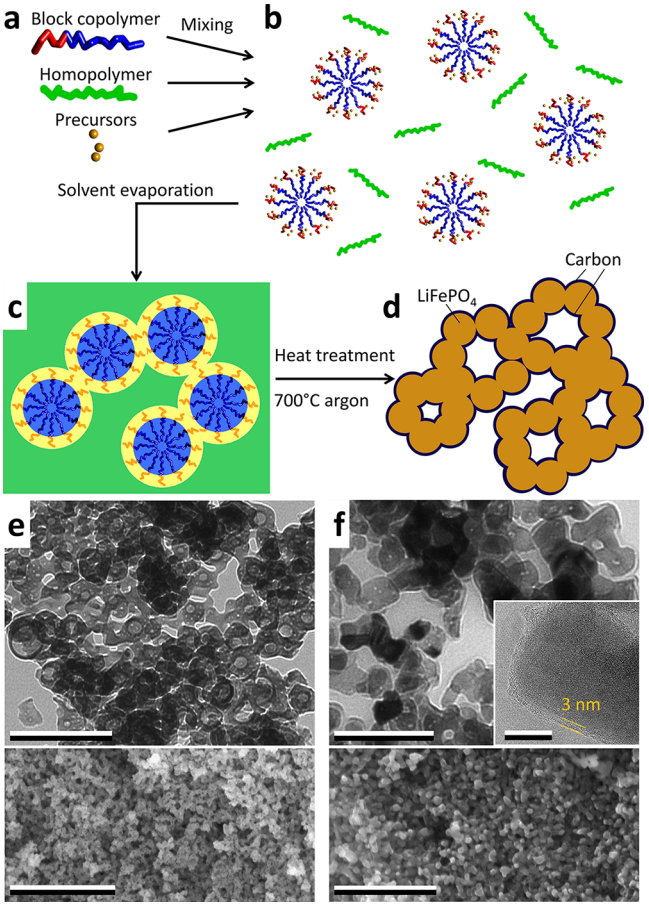

Figure 1. Scheme of the structure-formation process. (a) A BCP and a homopolymer are mixed with LFP precursors. (b) The BCP forms micelles in solution. LFP precursors complex with the hydrophilic block in the micellar coronas, whereas the homopolymer stays in solution. (c) During solvent evaporation, the homopolymer forms a solid matrix, freezing in the micellar morphology. (d) Annealing in an inert atmosphere crystallizes the LFP to form a network of LFP nanoparticles. The polymeric components are transformed into conductive carbon that covers the surface of the material. (e) The morphology of (c) can be visualized by electron microscopy when calcining the sample at a lower temperature in air, at which all polymers burn off, and the LFP precursors stay amorphous (top: TEM image, scale bar: 200 nm; bottom: SEM image, scale bar: 1 μm). (f) Electron microscopy images of the crystalline carbon-coated LFP network that results from high-temperature annealing in argon (top: TEM image, scale bar: 200 nm; inset: high-resolution TEM image, scale bar: 20 nm; bottom: SEM image, scale bar: 1 μm).

Briefly, it starts by mixing the sol−gel precursors (Li^+, Fe^{3+}, PO_4^{3-}) with a poly(styrene) homopolymer (35 kg/mol) and a high-molecular-weight poly(isoprene-*block*-ethylene oxide) block copolymer (BCP, 62 kg/mol) in tetrahydrofuran (THF). The slightly opaque mixture is then heated (50 °C) to evaporate the solvent and other volatile components, resulting in a monolithic material. When calcined in air at 500 °C, the organic components burn off, revealing a highly porous morphology that can be imaged by scanning electron microscopy (SEM) and transmission electron microscopy (TEM) (Figure 1e). These images reveal a dense agglomeration of interconnected hollow spheres with wall thicknesses on the 10 nm scale (Figure S1). X-ray diffraction (XRD) shows that the material remained amorphous when annealed in air (Figure S2).

Annealing the solidified material in an inert atmosphere instead (700 °C in argon) yields a black powder. SEM imaging displays an interconnected nanonetwork (Figure 1f) with a mesostructure similar to that of the precursors, albeit with a somewhat altered nanomorphology (Figure S3). High-resolution TEM reveals a uniform carbon layer with a thickness of approximately 3 nm covering the surface of the material (inset in Figure 1f and Figure S4).

The XRD data in Figure 2a confirms the formation of a pure LFP phase during annealing with an average crystallite size of 34 nm (derived from the Scherrer equation). This is in agreement with high-resolution TEM images that further show that the mesostructure is composed of interconnected single crystalline carbon-coated nanoparticles (around 30 nm in diameter, Figure S4).

The results of Figure 1e,f allow the derivation of a model for the structure-formation process during processing. Mixing the solvent, the precursor−sol, the BCP, and the homopolymer (Figure 1a), causes the aggregation of the BCP into micelles with poly(isoprene) cores and poly(ethylene oxide) shells,[44] while the homopolymer is dispersed in the solution (Figure 1b). Since the precursor−sol complexes with the hydrophilic poly(ethylene oxide) block,[45] it is contained within the micellar corona. Solvent evaporation maintains the micellar structure, which is then embedded within a homopolymer matrix, forming a dense network of spheres on the 10 nm scale (Figure 1c). To visualize this morphology, it is convenient to employ a heat treatment that burns off the polymers but prevents the inorganic components from crystallizing, thereby conserving the inorganic core−shell morphology (Figure 1e). However, a viable LFP battery cathode requires crystalline LFP and a condutive carbon coating. These can be achieved by annealing the dried material at a higher temperature in an oxygen-free atmosphere (Figure 1d). This results in LFP crystallization, as verified by XRD (Figure 2a) and high-resolution TEM (Figure S4). Under these conditions, the BCP and homopolymer carbonize, forming a conformal conducting layer on the LFP surface (Figures 1f and S4).

Experiments performed with an insufficient homopolymer content resulted in unconstrained crystal growth that damaged the mesostructure (Figure S5). This is in agreement with earlier observations, where the formation of a polymer-derived carbonaceous coating confines the crystallization process, thereby maintaining the BCP-induced nanomorphology.[46]

Raman measurements were employed to examine the molecular structure of the carbon coating (Figure 2b). The spectrum shows well pronounced peaks for the G-band (~1550 cm^{-1}) and D-band (~1350 cm^{-1}) of carbon with a peak area

DOI: 10.1021/acsami.7b12376
ACS Appl. Mater. Interfaces 2018, 10, 1646−1653

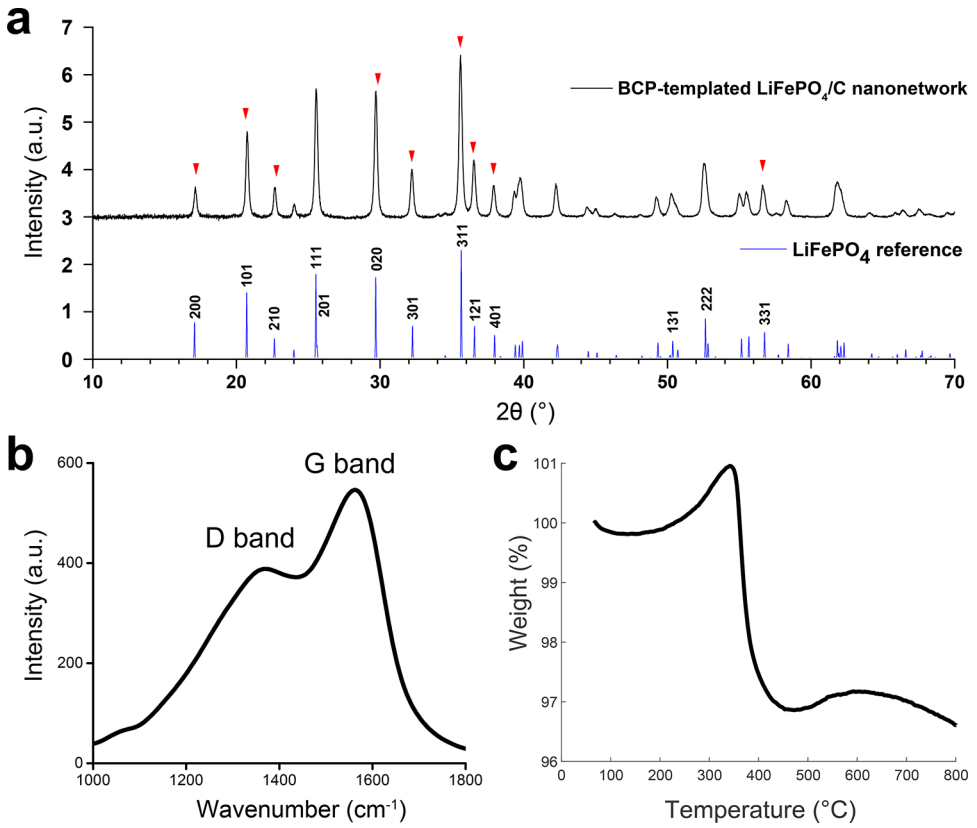

Figure 2. Characterization of the BCP-templated LFP/C nanonetwork. (a) XRD pattern of the material. All peaks can be matched to the $LiFePO_4$ reference pattern. Red triangles indicate peaks that were used for the Debye–Scherrer crystallite size determination. (b) Raman spectrum showing the D- and G-band of the carbon coating. (c) TGA data performed in air, showing the weight gain due to oxidation of LFP and the weight loss from burning off the carbon coating.

ratio (A_G/A_D) of approximately 0.35, indicating partial graphitization of the carbon layer. Physisorption measurements (Figure S6) further demonstrate the presence of pores in the carbon coating (3 to 4 nm in diameter). The amount of carbon in the LFP/C composite was determined by thermogravimetric analysis (TGA) measurements (Figure 2c). Taking the oxidation of $LiFePO_4$ to $Li_3Fe_2(PO_4)_3$ and Fe_2O_3 (resulting in a mass increase of 5.1 wt%) into account,[14,35,47] the composite had a carbon content of ~8.5 wt %.

As a control experiment, the same synthesis method without the structure-directing BCP was also performed. In the absence of the micellar templating of the precursor–sol (Figure 1b), the nontempated process also creates a nanoporous morphology (Figure S7), indicating that nanoporosity itself is a result of the sol–gel condensation process. The hollow spheres with features on the 10 nm scale (Figure 1e) are however only observed when a BCP was employed, confirming its role as a structure-directing agent. In particular, the lack of BCP compartmentalization of the precursor–sol led to a coarse agglomerated LFP/C composite, implying a loss of porosity upon annealing in an inert atmosphere (Figure S3). To rule out effects of an insufficient carbon coating, the amount of homopolymer in this experiment was adjusted so that the material synthesized with and without the BCP contained the same overall amount of polymer. This resulted in similar amounts of carbon that formed during pyrolysis, with a comparable degree of graphitization (Figure S8). In contrast to the BCP-templated process, the material synthesized in the absence of BCPs possesses a considerable fraction of carbon that is not in intimate contact with the surface of the LFP particles (inset in Figure S3d).

Our approach differs from earlier studies, where polymeric templating agents (such as commercially available triblock copolymers) were added to precursor solutions to introduce porosities in the carbon structure of the composite.[14,15,25,39] While these structure-directing agents can also be used to confine the LFP precursors to a nanosized morphology,[45] their low molecular weight however produces smaller self-assembled features. These are not retained during the high-temperature process required to crystallize the electrochemically active LFP phase (~700 °C).[48] In this case, crystal nucleation and growth results in a collapse of the self-assembled structure,[46] similar to the nanoporous morphology produced in the nontemplated synthesis (Figure S7).

The key of the here obtained morphology is the combination of the BCP's high molecular weight with a sufficiently strong chemical incompatibility of the amphiphilic blocks. Both of these features result in a self-assembled morphology with a larger characteristic length scale compared to conventional lower molecular weight structure-directing agents.[49] In contrast to previous soft-templating methods,[14,15,25,39] the BCP employed in this study allows the inorganic material to be templated at a length scale that matches the size of the LFP crystallites. While crystallization changed the detailed shape of the core–shell morphology (partially degrading the shell-like morphology observed in Figure 1e), our approach therefore delivers a fully crystallized compound with a controlled LFP nanomorphology. On the one hand, the self-assembled

DOI: 10.1021/acsami.7b12376
ACS Appl. Mater. Interfaces 2018, 10, 1646–1653

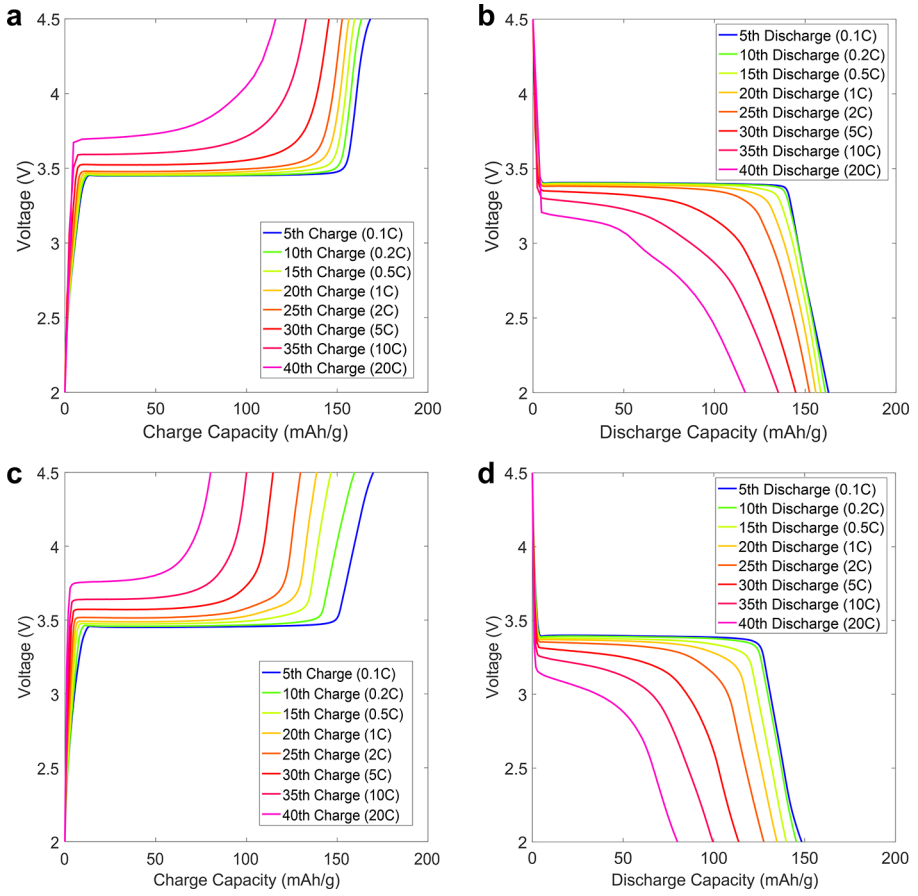

Figure 3. Galvanostatic charge (a,c) and discharge (b,d) curves for the BCP-templated (a,b) and the nontemplated (c,d) samples.

morphological features are large enough to prevent a collapse of the BCP-induced nanostructure (Figures 1f and S3a,c) during crystallization. On the other hand, the morphological dimensions of the BCP-micelle-induced structures are small compared to other templating processes, such as hollow spheres derived from spherical Li_3PO_4 templates,[32−34] (polymer) macrophase separation,[49] or hollow particles formed in solvothermal processes.[35] Consequently, the formation of a BCP-templated morphology on the length scale of the LFP crystallites provides short Li^+ diffusion distances within the intercalation material.

The use of a homopolymer as the main carbon source has the advantage that it is soluble in the same solvent (THF) as the BCP. Traditional carbon sources, such as sucrose[12] or resins[14] complex with the structure-directing agents, thereby affecting the self-assembled morphologies. The homopolymer however does not interact with the BCP and keeps the micelles unaltered. While the organic polymers have a lower carbon yield compared to other carbon sources,[12,14] the partially graphitized carbon layer improves electrical conductivity,[1,11,19] and its porosity enables efficient Li^+ transport across the coating.[25] In contrast to the nontemplated material, the BCP-templated nanonetwork possesses a uniform carbon coating (inset in Figure 1f and Figure S3) that enhances electron transport.[11]

2.2. Electrochemical Performance. The electrochemical performances of the templated and nontemplated materials were tested in a LIB. Galvanostatic charge/discharge curves for both samples show voltage plateaus corresponding to the two-phase lithiation mechanism of LFP[5], which are shifted at high current rates (Figure 3). Cyclic voltammetry data of the BCP-derived material exhibits a single oxidation and reduction peak each (Figure S9), in agreement with a one-step (de)lithiation process. The BCP-templated LFP/C composite demonstrates an excellent rate capability (Figure 4a) with a capacity of over 160 mAh/g at low rates (0.1 C) and a capacity of 117 mAh/g at a high rate of 20 C. In comparison, the nontemplated material exhibits an inferior rate performance with a capacity of 145 mAh/g at 0.1 C and approximately 80 mAh/g at 20 C.

Electrochemical impedance spectroscopy (EIS) shows that the BCP-templated nanonetwork has a lower impedance compared to that of the nontemplated reference material (Figure 4b). In particular, the (mass-normalized) charge-transfer resistance is significantly reduced in the BCP-templated material, by a factor of ∼6 (Tables S1 and S2). Furthermore, the cycling rate-dependence of the overpotential reveals kinetic differences between the templated and the nontemplated samples (Figure S10). While ohmic contributions are similar, the charge-transfer-related overpotential is considerably lowered for the BCP-templated sample (Table S3).

The BCP-templated LFP/C nanonetwork demonstrates excellent cyclability, reaching a capacity retention of over 92% after 1000 cycles at a charge/discharge rate of 1 C with an average Coulombic efficiency of 99.5% (Figure 4c).

The high initial capacities indicate that the active material is well-crystallized and has a low level of defects in its crystal structure.[37] The observation of a reduced charge-transfer resistance in the BCP-templated material compared to that in the nontemplated sample suggests that the smaller particle size of the BCP-templated LFP nanomorphology expedites the

DOI: 10.1021/acsami.7b12376
ACS Appl. Mater. Interfaces 2018, 10, 1646−1653

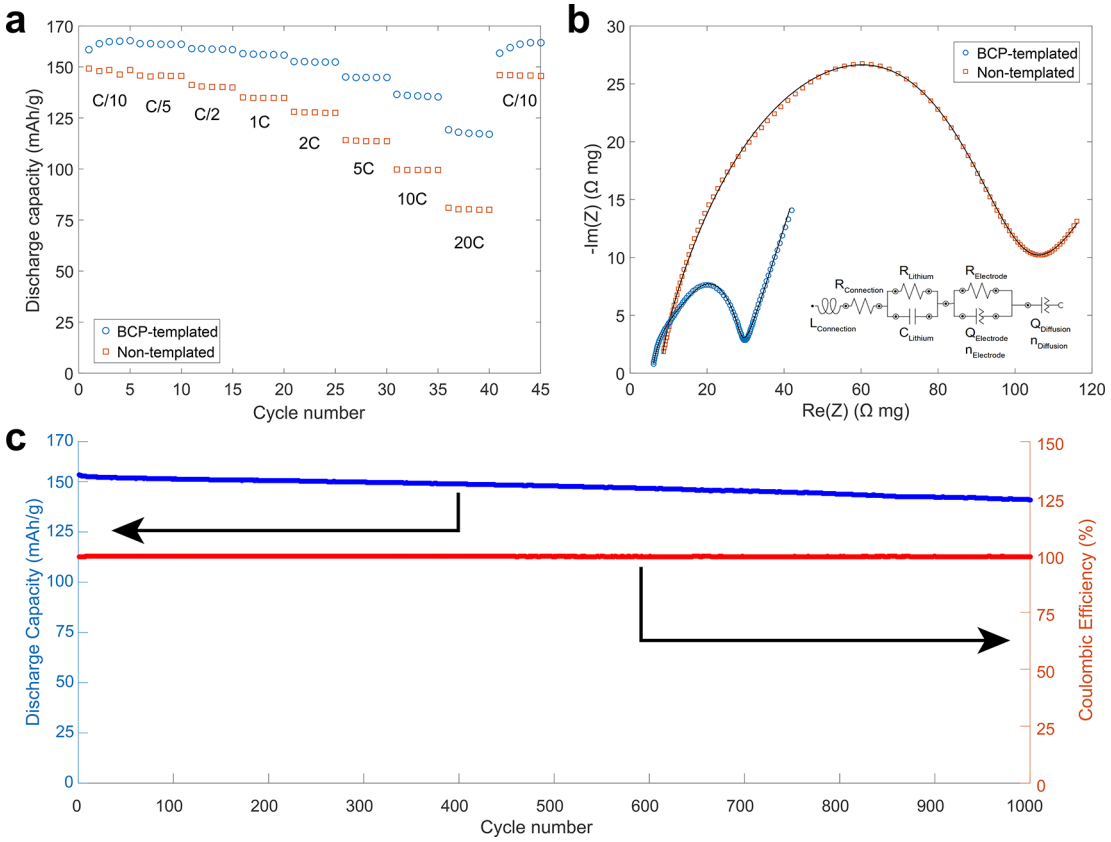

Figure 4. Electrochemical performance. (a) Rate capabilities of the BCP-templated LFP/C nanonetwork (blue circles) and the nontemplated reference material (red squares). (b) EIS measurements comparing the impedance of both electrode materials. Open symbols indicate measured data points, and lines correspond to fits to the equivalent circuit model shown in the inset. (c) Capacity retention (blue, left) and Coulombic efficiency (red, right) of the BCP-templated LFP/C nanonetwork over 1000 cycles at a rate of 1 C.

charge transfer across the electrode/electrolyte interface.[20] This explains the superior high rate performance of the LFP/C nanonetwork. The two-phase reaction mechanism of LFP usually involves phase transformations with significant structural rearrangements during cycling.[50] It has however been shown that downsizing LFP promotes a nonequilibrium solid solution behavior,[3,51] which contributes to the enhanced rate performance of the BCP-templated material as it bypasses the kinetically limiting nucleation and growth steps of secondary phases during (de)lithiation.[5,50] A general drawback of nanomaterials is that they can show pronounced side reactions.[1] Since LFP is well within the stability window of conventional electrolytes,[3] there are no apparent side reactions based on our electrochemistry data, ensuring a good cyclability and rate performance of the BCP-templated material.

The performance of the high-molecular-weight BCP-templated LFP/C nanonetwork is superior to other meso- and macroporous structures,[38,40] including those using a low-molecular-weight surfactant as structure-directing agent[14,15,39] (achieving capacities of ∼120 mAh/g or less at 5 C), stressing the importance of using higher-molecular-weight templating agents. The interconnected LFP/C nanonetwork shows better rate capabilities than electrodes made of LFP nanoparticles that have been combined with tailored (porous) carbon materials[12,13,16−18,25] (∼100 mAh/g at 5 C), indicating that efficient electron transport is facilitated by the homogeneous carbon coating created in situ by our procedure. The nanonetwork provides short diffusion distances and is highly accessible to the electrolyte, giving rise to fast Li^+ transport kinetics. The LFP/C composite therefore compares favorably to nanosized morphologies synthesized by hydro/solvothermal methods[26−31,35,36] and precipitation methods[32−34] (∼120 mAh/g at 10 C). Its performance of 135 mAh/g at 10 C relates closely to other LFP/C nanocomposites with primary particles of comparable size[23,24] (up to 135 mAh/g at 10 C) and lies in the range of structured materials that involve hard templates and complicated processing steps[41−43] (between 120 and 150 mAh/g at 10 C).

3. CONCLUSION

In conclusion, we present the synthesis of a nanostructured LFP/C cathode material with a morphology that is controlled by the self-assembly of a high molecular weight, highly amphiphilic BCP serving as a structure-directing agent. Compared to earlier work, our procedure has two salient features: (1) the correct choice of the structure-directing agent. The strong incompatibility of the amphiphilic BCP blocks creates stable complexes with the sol−gel precursor, while its high molecular weight prevents the crystallization process from destroying its self-assembled morphology during high-temperature processing, in contrast to conventional soft templates where the nanostructure collapses during crystallization. (2) The use of a homopolymer as a convenient carbon source that does not interact with the BCP complexes in solution. This maintains the integrity of the BCP−precursor aggregates on the 10 nm scale and gives rise to a highly conductive carbon coating that is sufficiently porous to provide access of Li^+ from the electrolyte to the LFP.

DOI: 10.1021/acsami.7b12376
ACS Appl. Mater. Interfaces 2018, 10, 1646−1653

The resulting LIB cathode material displays a large initial capacity, high capacity retention upon fast cycling, and an excellent cycle life. Since all processing steps (including mixing, evaporation, aging, and heat treatment) can be performed in the same container, our approach is a "one-pot" procedure,[46] enabling the scalability required for commercial manufacturing processes. Furthermore, a generally cheaper iron(III) source (instead of an iron(II) precursor)[4,24,31] was used since the polymers[48] and the in situ formed carbon coating[47] reduced the iron(III) precursor during pyrolysis.

Since this method delivers nanostructured electrode materials with a uniform carbon coating based on a rather generic sol–gel chemistry, it should be applicable to a wide range of battery electrode materials (anodes as well as cathodes). Particularly interesting candidates for this approach are olivine derivatives or other polyanionic compounds (e.g., $LiMnPO_4$), which suffer from even lower electrical and ionic conductivities than LFP.[5,52]

4. EXPERIMENTAL SECTION

4.1. Chemicals. Iron(III) acetylacetonate ($Fe(acac)_3$, ≥ 99.9%), tetrahydrofuran (THF, ≥ 99.9%, stabilized by 250 ppm BHT), lithium chloride solution (0.5 M LiCl in THF), concentrated hydrochloric acid (37 wt % HCl in H_2O), concentrated phosphoric acid (85 wt % H_3PO_4 in H_2O, 99.99%), 1-methyl-2-pyrrolidinone (NMP, anhydrous, 99.5%), polystyrene (PS, 35 kg/mol), 1.0 M $LiPF_6$ in 1:1 (v:v) ethylene carbonate (EC)/ethyl methyl carbonate (EMC) (battery grade), and lithium ribbon (thickness = 0.75 mm) were purchased from Sigma-Aldrich. Poly(isoprene(1,4-addition)-*block*-ethylene oxide) (PI-*b*-PEO) with a molecular weight of 62 kg/mol (50 kg/mol PI and 12 kg/mol PEO) was purchased from Polymer Source. All chemicals were used as received.

4.1.1. Synthesis of the LFP/C Nanonetwork. $Fe(acac)_3$ (1342 mg) was first dissolved in THF (36 mL). 0.5 M LiCl in THF (7.84 mL), concentrated hydrochloric acid (315 μL), and a BCP solution (300 mg PI-*b*-PEO dissolved in 6 mL of THF) were then added, and the mixture was stirred overnight. Concentrated phosphoric acid (260 μL) and a homopolymer solution (500 mg of PS dissolved in 10 mL of THF) were then added, and the precursor solution (ca. 60 mL in total) was stirred for 30 min. The addition of phosphoric acid initiated a change from a transparent, dark-red solution to a slightly opaque, orange-colored mixture. The described synthesis resulted in equimolar ratios for Fe, PO_4, and HCl. A molar excess of approximately 3% lithium was used to ensure phase purity. We employed a 2:1 weight ratio of LFP to BCP and a 5:3 ratio of homopolymer to BCP.

The fabrication protocol for the nontemplated sol–gel-derived LFP material was identical to that for the templated material, except that the BCP solution was replaced by an additional amount of homopolymer solution (800 mg of PS dissolved in 16 mL of THF).

The precursor solutions were subsequently transferred to a Petri dish for evaporation. This Petri dish was situated in a larger half-open Petri dish on a hot plate set to 50 °C to ensure similar evaporation conditions for different batches.[49] After solvent evaporation was complete, the material was aged at 70 °C under vacuum overnight before high-temperature calcination. To image the structure of the solidified precursors, the samples were calcined at 500 °C in air for 1 h (2 °C/min ramp), thereby burning off all organic compounds. The electrochemically active LFP/C composites were obtained by transferring the aged materials to a tube furnace. They were heated under flowing argon to 500 °C (5 °C/min ramp) and held for 2 h before being annealed at 700 °C (5 °C/min ramp) for another 2 h.

4.2. Characterization Techniques. The mesostructure of the samples was imaged with a Tescan Mira 3 LMH scanning electron microscope (SEM). X-ray diffraction (XRD) was performed using a Rigaku Ultima IV with a copper target. LaB_6 was used as an external reference to obtain the instrumental broadening. Thermogravimetric analysis (TGA) was performed with a Mettler Toledo system using an Al_2O_3 crucible and a temperature range of 60 to 800 °C with a heating rate of 2 °C/min. Raman measurements were performed on a custom-built Raman setup employing a 100 mW 633 nm laser. Transmission electron microscopy (TEM) images were obtained at room temperature using a FEI Tecnai Spirit with a 120 kV LaB_6 emitter. Images were acquired using a Veleta charge-coupled device (CCD) sensor. High-resolution TEM images were obtained using a JEOL 3000 operated at 250 kV. Physisorption measurements for the calculation of specific surface areas (BET) and pore size distributions (BJH) were conducted with a Micromeritics Gemini V Surface Area Analyzer using nitrogen as the adsorbate.

4.3. Electrode Fabrication and Battery Assembly. To fabricate electrode films for LIBs, the LFP/C composite was mixed with conductive carbon black (Timcal Super C65) and a polyvinylidene fluoride binder (PVdF, Kynar) in the weight ratio of 75:15:10. NMP (2.5 μL per gram of mixture) was added and mixed with these components to produce a paste that was cast onto aluminum foils. The average mass loading of the active material was 0.75 ± 0.24 mg/cm^2. Circular electrodes (1/2 in. in diameter) were cut and dried at 80 °C under vacuum overnight. Afterward, they were transferred to an argon-filled glovebox (MBraun Labmaster Pro) where they were assembled in Swagelok cells with lithium metal (thickness = 0.75 mm) as the counter electrode. 1.0 M $LiPF_6$ in 1:1 (v:v) EC/EMC was used as the electrolyte and a glass fiber disc (Whatman, grade GF/B) was used as a separator. Galvanostatic cycling and cyclic voltammetry tests were conducted at room temperature with an Arbin BT 2043 to investigate the rate performance (voltage range from 2 to 4.5 V vs Li/Li^+) and the cycle life (voltage range from 2 to 4.3 V vs Li/Li^+) of the cathodes. Electrochemical impedance spectroscopy (EIS) was performed using a Metrohm Autolab PGSTAT302N. After the galvanostatic rate performance tests were completed, the cells were charged to 4.2 V and subsequently discharged at a rate of approximately 1 C to 3.385 V (within the two-phase plateau of the discharge process). Potentiostatic EIS measurements were then performed at this voltage using an amplitude of 10 mV. A frequency range from 1 MHz to 1 Hz was employed with 20 data points taken per decade.

■ ASSOCIATED CONTENT

Supporting Information

The Supporting Information is available free of charge on the ACS Publications website at DOI: 10.1021/acsami.7b12376.

Size distributions of characteristic features of the BCP-derived morphology; XRD patterns of the BCP-templated sample for different heat treatments; SEM and TEM images of the BCP-templated and the nontemplated samples; high-resolution TEM images; SEM images of samples with insufficient carbon coating; physisorption data and pore size distributions; SEM and TEM images of the precursor structure of the non-templated sample; Raman and TGA measurements of the nontemplated sample; cyclic voltammetry data; cycling rate dependence of charge and discharge overpotentials, including fits according to different models; fit parameters and a detailed description of the underlying models (PDF)

■ AUTHOR INFORMATION

Corresponding Authors

*E-mail: xiao.hua@unifr.ch (X.H.)
*E-mail: ullrich.steiner@unifr.ch (U.S.)

ORCID

Michael G. Fischer: 0000-0002-0519-5463
Xiao Hua: 0000-0002-8673-5678
Bodo D. Wilts: 0000-0002-2727-7128
Elizabeth Castillo-Martínez: 0000-0002-8577-9572

DOI: 10.1021/acsami.7b12376
ACS Appl. Mater. Interfaces 2018, 10, 1646–1653

Ullrich Steiner: 0000-0001-5936-339X

Notes

The authors declare no competing financial interest.

■ ACKNOWLEDGMENTS

We thank Preston H. Sutton and Jonathan H. W. Lim for useful discussions. Funding from the Swiss National Science Foundation through the NRP70 (153764) and Ambizione (BDW: 168223) programs, and funding from the Adolphe Merkle Foundation are gratefully acknowledged.

■ REFERENCES

(1) Bruce, P. G.; Scrosati, B.; Tarascon, J.-M. Nanomaterials for Rechargeable Lithium Batteries. *Angew. Chem., Int. Ed.* **2008**, *47*, 2930−2946.
(2) Goodenough, J. B.; Kim, Y. Challenges for Rechargeable Li Batteries. *Chem. Mater.* **2010**, *22*, 587−603.
(3) Wagemaker, M.; Mulder, F. M. Properties and Promises of Nanosized Insertion Materials for Li-Ion Batteries. *Acc. Chem. Res.* **2013**, *46*, 1206−1215.
(4) Whittingham, M. S. Ultimate Limits to Intercalation Reactions for Lithium Batteries. *Chem. Rev.* **2014**, *114*, 11414−11443.
(5) Wang, J.; Sun, X. Olivine $LiFePO_4$: The Remaining Challenges for Future Energy Storage. *Energy Environ. Sci.* **2015**, *8*, 1110−1138.
(6) Padhi, A. K.; Nanjundaswamy, K. S.; Goodenough, J. B. Phospho-Olivines as Positive-Electrode Materials for Rechargeable Lithium Batteries. *J. Electrochem. Soc.* **1997**, *144*, 1188−1194.
(7) Chung, S.-Y.; Bloking, J. T.; Chiang, Y.-M. Electronically Conductive Phospho-Olivines as Lithium Storage Electrodes. *Nat. Mater.* **2002**, *1*, 123−128.
(8) Park, M.; Zhang, X.; Chung, M.; Less, G. B.; Sastry, A. M. A Review of Conduction Phenomena in Li-Ion Batteries. *J. Power Sources* **2010**, *195*, 7904−7929.
(9) Kang, B.; Ceder, G. Battery Materials for Ultrafast Charging and Discharging. *Nature* **2009**, *458*, 190−193.
(10) Huang, H.; Yin, S.-C.; Nazar, L. F. Approaching Theoretical Capacity of $LiFePO_4$ at Room Temperature at High Rates. *Electrochem. Solid-State Lett.* **2001**, *4*, A170−A172.
(11) Doeff, M. M.; Hu, Y.; McLarnon, F.; Kostecki, R. Effect of Surface Carbon Structure on the Electrochemical Performance of $LiFePO_4$. *Electrochem. Solid-State Lett.* **2003**, *6*, A207−A209.
(12) Ni, H.; Liu, J.; Fan, L.-Z. Carbon-coated $LiFePO_4$-Porous Carbon Composites as Cathode Materials for Lithium Ion Batteries. *Nanoscale* **2013**, *5*, 2164−2168.
(13) Cheng, F.; Wang, S.; Lu, A.-H.; Li, W.-C. Immobilization of Nanosized $LiFePO_4$ Spheres by 3D Coralloid Carbon Structure with Large Pore Volume and Thin Walls for High Power Lithium-Ion Batteries. *J. Power Sources* **2013**, *229*, 249−257.
(14) Wu, R.; Xia, G.; Shen, S.; Zhu, F.; Jiang, F.; Zhang, J. Soft-Templated $LiFePO_4$/Mesoporous Carbon Nanosheets (LFP/meso-CNSs) Nanocomposite as the Cathode Material of Lithium Ion Batteries. *RSC Adv.* **2014**, *4*, 21325−21331.
(15) Sun, S.; Ghimbeu, C. M.; Janot, R.; Le Meins, J.-M.; Cassel, A.; Davoisne, C.; Masquelier, C.; Vix-Guterl, C. One-Pot Synthesis of $LiFePO_4$-Carbon Mesoporous Composites for Li-Ion Batteries. *Microporous Mesoporous Mater.* **2014**, *198*, 175−184.
(16) Zhou, Y.; Wang, J.; Hu, Y.; O'Hayre, R.; Shao, Z. A Porous $LiFePO_4$ and Carbon Nanotube Composite. *Chem. Commun.* **2010**, *46*, 7151−7153.
(17) Yang, J.; Wang, J.; Tang, Y.; Wang, D.; Xiao, B.; Li, X.; Li, R.; Liang, G.; Sham, T.-K.; Sun, X. In Situ Self-Catalyzed Formation of Core-Shell $LiFePO_4$@CNT Nanowires for High Rate Performance Lithium-Ion Batteries. *J. Mater. Chem. A* **2013**, *1*, 7306−7311.
(18) Yang, J.; Wang, J.; Tang, Y.; Wang, D.; Li, X.; Hu, Y.; Li, R.; Liang, G.; Sham, T.-K.; Sun, X. $LiFePO_4$-Graphene as a Superior Cathode Material for Rechargeable Lithium Batteries: Impact of Stacked Graphene and Unfolded Graphene. *Energy Environ. Sci.* **2013**, *6*, 1521−1528.
(19) Song, J.; Sun, B.; Liu, H.; Ma, Z.; Chen, Z.; Shao, G.; Wang, G. Enhancement of the Rate Capability of $LiFePO_4$ by a New Highly Graphitic Carbon-Coating Method. *ACS Appl. Mater. Interfaces* **2016**, *8*, 15225−15231.
(20) Bai, P.; Bazant, M. Z. Charge Transfer Kinetics at the Solid-Solid Interface in Porous Electrodes. *Nat. Commun.* **2014**, *5*, 3585.
(21) Hsu, K.-F.; Tsay, S.-Y.; Hwang, B.-J. Synthesis and Characterization of Nano-Sized $LiFePO_4$ Cathode Materials Prepared by a Citric Acid-Based Sol-Gel Route. *J. Mater. Chem.* **2004**, *14*, 2690−2695.
(22) Dominko, R.; Bele, M.; Goupil, J.-M.; Gaberscek, M.; Hanzel, D.; Arcon, I.; Jamnik, J. Wired Porous Cathode Materials: A Novel Concept for Synthesis of $LiFePO_4$. *Chem. Mater.* **2007**, *19*, 2960−2969.
(23) Delacourt, C.; Poizot, P.; Levasseur, S.; Masquelier, C. Size Effects on Carbon-Free $LiFePO_4$ Powders: The Key to Superior Energy Density. *Electrochem. Solid-State Lett.* **2006**, *9*, A352−A355.
(24) Wang, Y.; Wang, Y.; Hosono, E.; Wang, K.; Zhou, H. The Design of a $LiFePO_4$/Carbon Nanocomposite With a Core-Shell Structure and Its Synthesis by an In-Situ Polymerization Restriction Method. *Angew. Chem., Int. Ed.* **2008**, *47*, 7461−7465.
(25) Wu, X.-L.; Jiang, L.-Y.; Cao, F.-F.; Guo, Y.-G.; Wan, L.-J. $LiFePO_4$ Nanoparticles Embedded in a Nanoporous Carbon Matrix: Superior Cathode Material for Electrochemical Energy-Storage Devices. *Adv. Mater.* **2009**, *21*, 2710−2714.
(26) Saravanan, K.; Balaya, P.; Reddy, M. V.; Chowdari, B. V. R.; Vittal, J. J. Morphology Controlled Synthesis of $LiFePO_4$/C Nanoplates for Li-Ion Batteries. *Energy Environ. Sci.* **2010**, *3*, 457−463.
(27) Nan, C.; Lu, J.; Chen, C.; Peng, Q.; Li, Y. Solvothermal Synthesis of Lithium Iron Phosphate Nanoplates. *J. Mater. Chem.* **2011**, *21*, 9994−9996.
(28) Pei, B.; Yao, H.; Zhang, W.; Yang, Z. Hydrothermal Synthesis of Morphology-Controlled $LiFePO_4$ Cathode Material for Lithium-Ion Batteries. *J. Power Sources* **2012**, *220*, 317−323.
(29) Ma, Z.; Shao, G.; Fan, Y.; Wang, G.; Song, J.; Liu, T. Tunable Morphology Synthesis of $LiFePO_4$ Nanoparticles as Cathode Materials for Lithium Ion Batteries. *ACS Appl. Mater. Interfaces* **2014**, *6*, 9236−9244.
(30) Lou, X.; Zhang, Y. Synthesis of $LiFePO_4$/C Cathode Materials with Both High-Rate Capability and High Tap Density for Lithium-Ion Batteries. *J. Mater. Chem.* **2011**, *21*, 4156−4160.
(31) Sun, C.; Rajasekhara, S.; Goodenough, J. B.; Zhou, F. Monodisperse Porous $LiFePO_4$ Microspheres for a High Power Li-Ion Battery Cathode. *J. Am. Chem. Soc.* **2011**, *133*, 2132−2135.
(32) Lee, M.-H.; Kim, J.-Y.; Song, H.-K. A Hollow Sphere Secondary Structure of $LiFePO_4$ Nanoparticles. *Chem. Commun.* **2010**, *46*, 6795−6797.
(33) Lee, M.-H.; Kim, T.-H.; Kim, Y. S.; Song, H.-K. Precipitation Revisited: Shape Control of $LiFePO_4$ Nanoparticles by Combinatorial Precipitation. *J. Phys. Chem. C* **2011**, *115*, 12255−12259.
(34) Yang, S.; Hu, M.; Xi, L.; Ma, R.; Dong, Y.; Chung, C. Y. Solvothermal Synthesis of Monodisperse $LiFePO_4$ Micro Hollow Spheres as High Performance Cathode Material for Lithium Ion Batteries. *ACS Appl. Mater. Interfaces* **2013**, *5*, 8961−8967.
(35) Zheng, Z.; Pang, W. K.; Tang, X.; Jia, D.; Huang, Y.; Guo, Z. Solvothermal Synthesis and Electrochemical Performance of Hollow $LiFePO_4$ Nanoparticles. *J. Alloys Compd.* **2015**, *640*, 95−100.
(36) Peng, L.; Zhao, Y.; Ding, Y.; Yu, G. Self-Assembled $LiFePO_4$ Nanowires with High Rate Capability for Li-Ion Batteries. *Chem. Commun.* **2014**, *50*, 9569−9572.
(37) Jensen, K. M. Ø.; Christensen, M.; Gunnlaugsson, H. P.; Lock, N.; Bøjesen, E. D.; Proffen, T.; Iversen, B. B. Defects in Hydrothermally Synthesized $LiFePO_4$ and $LiFe_{1-x}Mn_xPO_4$ Cathode Materials. *Chem. Mater.* **2013**, *25*, 2282−2290.
(38) Doherty, C. M.; Caruso, R. A.; Smarsly, B. M.; Drummond, C. J. Colloidal Crystal Templating to Produce Hierarchically Porous $LiFePO_4$ Electrode Materials for High Power Lithium Ion Batteries. *Chem. Mater.* **2009**, *21*, 2895−2903.

DOI: 10.1021/acsami.7b12376
ACS Appl. Mater. Interfaces 2018, 10, 1646−1653

(39) Doherty, C. M.; Caruso, R. A.; Smarsly, B. M.; Adelhelm, P.; Drummond, C. J. Hierarchically Porous Monolithic $LiFePO_4$/Carbon Composite Electrode Materials for High Power Lithium Ion Batteries. *Chem. Mater.* **2009**, *21*, 5300−5306.
(40) Hou, Y.; Wang, X.; Zhu, Y.; Hu, C.; Chang, Z.; Wu, Y.; Holze, R. Macroporous $LiFePO_4$ as a Cathode for an Aqueous Rechargeable Lithium Battery of High Energy Density. *J. Mater. Chem. A* **2013**, *1*, 14713−14718.
(41) Lim, S.; Yoon, C. S.; Cho, J. Synthesis of Nanowire and Hollow $LiFePO_4$ Cathodes for High-Performance Lithium Batteries. *Chem. Mater.* **2008**, *20*, 4560−4564.
(42) Wang, G.; Liu, H.; Liu, J.; Qiao, S.; Lu, G. M.; Munroe, P.; Ahn, H. Mesoporous $LiFePO_4$/C Nanocomposite Cathode Materials for High Power Lithium Ion Batteries with Superior Performance. *Adv. Mater.* **2010**, *22*, 4944−4948.
(43) Hill, M. R.; Wilson, G. J.; Bourgeois, L.; Pandolfo, A. G. High Surface Area Templated $LiFePO_4$ from a Single Source Precursor Molecule. *Energy Environ. Sci.* **2011**, *4*, 965−972.
(44) Hamley, I. *Block Copolymers in Solution: Fundamentals and Applications*; John Wiley & Sons: Chichester, UK, 2005.
(45) Yang, P.; Zhao, D.; Margolese, D. I.; Chmelka, B. F.; Stucky, G. D. Generalized Syntheses of Large-Pore Mesoporous Metal Oxides with Semicrystalline Frameworks. *Nature* **1998**, *396*, 152−155.
(46) Lee, J.; Christopher Orilall, M.; Warren, S. C.; Kamperman, M.; DiSalvo, F. J.; Wiesner, U. Direct Access to Thermally Stable and Highly Crystalline Mesoporous Transition-Metal Oxides with Uniform Pores. *Nat. Mater.* **2008**, *7*, 222−228.
(47) Ping Ong, S.; Wang, L.; Kang, B.; Ceder, G. Li−Fe−P−O2 Phase Diagram from First Principles Calculations. *Chem. Mater.* **2008**, *20*, 1798−1807.
(48) Ravet, N.; Gauthier, M.; Zaghib, K.; Goodenough; Mauger, A.; Gendron, F.; Julien. Mechanism of the Fe3+ Reduction at Low Temperature for $LiFePO_4$ Synthesis from a Polymeric Additive. *Chem. Mater.* **2007**, *19*, 2595−2602.
(49) Fischer, M. G.; Hua, X.; Wilts, B. D.; Gunkel, I.; Bennett, T. M.; Steiner, U. Mesoporous Titania Microspheres with Highly Tunable Pores as an Anode Material for Lithium Ion Batteries. *ACS Appl. Mater. Interfaces* **2017**, *9*, 22388−22397.
(50) Liu, H.; Strobridge, F. C.; Borkiewicz, O. J.; Wiaderek, K. M.; Chapman, K. W.; Chupas, P. J.; Grey, C. P. Capturing Metastable Structures during High-Rate Cycling of $LiFePO_4$ Nanoparticle Electrodes. *Science* **2014**, *344*, 1252817.
(51) Yamada, A.; Koizumi, H.; Nishimura, S.-i.; Sonoyama, N.; Kanno, R.; Yonemura, M.; Nakamura, T.; Kobayashi, Y. Room-Temperature Miscibility Gap in Li_xFePO_4. *Nat. Mater.* **2006**, *5*, 357−360.
(52) Oh, S.-M.; Myung, S.-T.; Park, J. B.; Scrosati, B.; Amine, K.; Sun, Y.-K. Double-Structured $LiMn_{0.85}Fe_{0.15}PO_4$ Coordinated with $LiFePO_4$ for Rechargeable Lithium Batteries. *Angew. Chem., Int. Ed.* **2012**, *51*, 1853−1856.

DOI: 10.1021/acsami.7b12376
ACS Appl. Mater. Interfaces 2018, 10, 1646−1653